

Minor Chemistry Changes Alter Surface Hydration to Control Fibronectin Adsorption and Assembly into Nanofibrils

Mateusz K. Bieniek, Virginia Llopis-Hernandez, Katie Douglas, Manuel Salmeron-Sanchez,* and Christian D. Lorenz*

Fibronectin (FN) is a large glycoprotein which links and transmits signals between the cell's cytoskeleton and the extracellular matrix. FN organization into fibrils and then fibrillogenesis can be induced with the right substrate, such as poly(ethyl acrylate) (PEA), on which FN becomes extended. Interestingly, the almost identical polymer poly(methyl acrylate) (PMA), which has one less methylene bridge ($-\text{CH}_2-$), does not cause fibrillogenesis. To investigate the difference in FN behavior on PEA and PMA, the two substrates are modeled using ethyl acrylate (EA) and methyl acrylate (MA) functionalized self-assembled monolayers (SAMs). It is confirmed experimentally that the EA and MA SAMs exhibit a similar behavior in vitro to the polymers in terms of fibronectin fibrillogenesis, domain exposure, and cell adhesion. All-atom molecular dynamics simulations of the FNIII 9-10 domains interacting with each SAM show the adsorption of these two domains on EA SAMs and no adsorption on MA SAMs. Consistently, the experiments show that FN fibrillogenesis takes place on EA SAMs but not on MA SAMs. It is found that the extra methylene group in the EA headgroup leads to more motion within the headgroup that results in a markedly less dense hydration layer, which facilitates FN fibrillogenesis.

1. Introduction

Fibronectin (FN) is a large mosaic extracellular matrix (ECM) glycoprotein that is essential for development.^[1] It affects important cellular processes including differentiation,^[2] cell growth,^[3] and proliferation.^[4] FN is a dimer consisting of two polypeptide chains linked via the cysteines at the carbonyl-terminal. Each polypeptide chain has three distinctive domain types (labeled I, II, and III). A single polypeptide contains 12 type I, only 2 type II, and 15–17 type III domains, depending on the slicing. The domains bind a variety of biomolecules including integrins, collagen/gelatin, heparin, fibrin, growth factors and, crucially for fibrillogenesis, fibronectin itself.^[5,6] The FNIII 9th and 10th domains contain the PHSRN motif (the synergy region) and the RGD motif (Arg–Gly–Asp)^[7], respectively, which both play key roles in the binding of FN to integrins, including $\alpha 5 \beta 1$.^[8,9]

FNs bind to integrins and then undergo fibrillogenesis, becoming a part of the ECM, where FN acts as a reservoir for growth factors.^[10] The formation and behavior of these FN fibrils plays an important role in the developmental processes, tissue homeostasis, fibrosis, and cancer.^[11] The complexity of this process is further compounded by the dynamic behavior of the FN networks.^[11]


Fibronectin exists in two main types: soluble and insoluble. The insoluble type is produced around cells and is incorporated into ECM immediately, whereas the soluble type is produced by hepatocytes and diffuses in the plasma. Here, we focus on the soluble type FN which assumes a compact native quaternary conformation. The FN compact conformation results from interactions between FN I 4 and FN III 3 of the same subunit, and FN III 2-3 and FN III 12-14 of the different subunits^[12] (the compact conformation is discussed in detail in the review^[13]). This compact conformation makes FN–FN bindings less accessible, thus preventing fibrillogenesis.^[14–16]

In vivo, the formation of the matrix takes place when the integrins exert forces on bound FN which changes its quaternary structure to an extended conformation, thus allowing the FN–FN associations to take place.^[17,18] These forces are exerted

M. K. Bieniek, Dr. C. D. Lorenz
Department of Physics
King's College London
London WC2R 2LS, UK
E-mail: chris.lorenz@kcl.ac.uk

M. K. Bieniek
Francis Crick Institute
1 Midland Road, London NW1 1AT, UK

Dr. V. Llopis-Hernandez, K. Douglas, Prof. M. Salmeron-Sanchez
Centre for the Cellular Microenvironment
University of Glasgow
Glasgow G12 8LT, UK
E-mail: manuel.salmeron-sanchez@glasgow.ac.uk

 The ORCID identification number(s) for the author(s) of this article can be found under <https://doi.org/10.1002/adts.201900169>

© 2019 The Authors. Published by WILEY-VCH Verlag GmbH & Co. KGaA, Weinheim. This is an open access article under the terms of the Creative Commons Attribution License, which permits use, distribution and reproduction in any medium, provided the original work is properly cited.

DOI: 10.1002/adts.201900169

through cytoskeleton reorganization, whose loss of contractility via blockade of Rho GTPase leads to reduced fibrillogenesis.^[18,19] FN binding is followed by integrin clustering which is believed to bring FNs within sufficient proximity for self-association.^[19] The motif RGD is necessary for the initiation of the FN matrix assembly, which is due to the importance of the motif in the integrin binding.^[20] Further information regarding cell-driven fibrillogenesis can be found in the review by Singh et al.^[21]

Recent studies^[2,22–24] showed that FN fibrillogenesis can take place without the presence of cells. When FN interacts with certain polymeric substrates, such as poly(ethyl acrylate) (PEA), protein matrix assembly is observed. The formation of the FN matrix is important for cell fate and behavior, which supports specific solid-phase presentation of growth factors (through the FNIII 12–14 heparin-binding domain) and enhances cell differentiation on the fully formed matrix.^[2,24] Based on this phenomenon, a novel technology has been developed for ECM-mimetic biomaterial construction with potential applications in tissue engineering. We recently showed that this technology promoted bone regeneration in critical-sized bone defects in a veterinary patient.^[25] Surprisingly, a chemically similar polymer, poly(methyl acrylate), with only one fewer methylene bridge ($-\text{CH}_2-$) in its side chain does not trigger fibrillogenesis. The length of the side chain of the poly(alkyl acrylates) family (to which PEA belongs) has been further investigated showing that longer side chains increased the exposure of the integrin binding domains, highlighting the importance of the hydrophobicity in the process.^[26]

In this manuscript, self-assembled monolayers (SAMs) consisting of alkanethiols on gold which we functionalized with the ethyl acrylate, EA ($-\text{C}(=\text{O})\text{OCH}_2\text{CH}_3$) and methyl acrylate, MA ($-\text{C}(=\text{O})\text{OCH}_3$) side chains were used to mimic the properties of the polymers PEA and poly(methyl acrylate) (PMA). To verify these model surfaces, we compare the adsorption, epitope availability, and cell adhesion of fibronectin on the polymers and SAMs systems. Also, all-atom molecular dynamics simulations have been used to gain atomistic detail regarding how the FNIII domains 9 and 10 interact with the EA and MA SAMs.

Molecular-scale computer simulations have been increasingly used to investigate the adsorption of proteins to a variety of interfaces. Simulations have been used to investigate the adsorption of various domains of fibronectin to bare,^[27–31] SAMs-functionalized,^[32–35] and polymeric^[36–38] surfaces. Of these studies, the simulations of the RGD and PHSRN containing FNIII domains on SAMs have been used to investigate $-\text{COOH}$ (in which some are deprotonated resulting in a negatively charged interface), $-\text{NH}_2$ (in which some are protonated resulting in a positively charged interface), $-\text{OH}$ (hydrophilic) and $-\text{CH}_3$ (hydrophobic) terminated SAMs. Monte Carlo simulations of the FNIII 7–10 domains showed that they adsorb to the two charged interfaces^[32,34] and the hydrophobic interface,^[34] but not the hydrophilic interface.^[34] These Monte Carlo simulations show that the RGD and PHSRN motifs are more available when adsorbed to the positively charged surfaces and more buried when adsorbed to negatively charged and hydrophobic surfaces.^[32,34] Molecular dynamics simulations of the FNIII 9th and 9th and 10th domains were performed on the same four interfaces.^[33] These simulations show that both peptides adsorb to all four interfaces. The RGD and PHSRN motifs are found to be most available on the positively charged and hydrophilic interfaces. Molec-

ular dynamics simulations of the FNIII 8–10th domains with the same interfaces show much the same behavior with respect to the binding to all interfaces and the availability of the RGD and PHSRN motifs, with the exception that the availability of these two domains was best on the positively charged surfaces, and less available on the hydrophilic surface.^[35]

In this study, we have carried out all-atom molecular dynamics simulations studying the interaction of the FNIII 9th and 10th domains with EA and MA SAMs, totaling four 500 ns-long simulations. We observed adsorption of the 9th domain on the EA SAMs but not on MA SAMs, and no adsorption of the 10th domain in either. We find that both of the RGD and PHSRN motifs are available for cell binding on the EA SAMs. The analysis of the adsorbing residues shows that the same residue regions drive the adsorption on the EA SAMs. We reason that the difference in adsorption is due to the water hydration of the surface, which we show to be significantly denser in the case of MA SAMs.

2. Experimental Section

2.1. Self-Assembled Monolayers

In the laboratory, SAMs surfaces mimicking the polymers were created from alkanethiols 1-dodecanethiol ($\text{HS}-(\text{CH}_2)_{10}-\text{COOCH}_3$) for MA and for ($\text{HS}-(\text{CH}_2)_{10}-\text{COOCH}_2\text{CH}_3$) EA (ProChimia). Au-coated glass coverslips (Fisher Scientific) were prepared by deposition of thin films of Ti (150 Å) followed by Au (150 Å) using a high vacuum evaporator (MEB 550S Electron beam evaporator from Plassys) at a deposition rate of 2 Å s^{-1} and a chamber base-pressure of 2×10^{-6} Torr. Glass coverslips were cleaned with RCA solution at 65°C for 15 min, rinsed with deionized H₂O, rinsed with 95% ethanol, and dried under a stream of N₂ prior to metal deposition. Freshly prepared Au-coated surfaces were immersed in alkanethiol solutions (1 mM in absolute ethanol), and SAMs were allowed to assemble overnight. SAMs were rinsed in 95% ethanol, dried under N₂, and allowed to equilibrate in DPBS prior to incubation in FN solutions. Surfaces were validated by water contact angle measurements (Dataphysics OCA). Chemistry of the surfaces were analyzed using water contact angle (WCA) and X-ray photoelectron spectroscopy (XPS). WCA analysis was carried out on PEA or PMA surfaces alone and on FN-coated surfaces. For each condition, the static contact angle (SCA), advancing contact angle (ACA), and receding contact angle (RCA) were determined ($n = 9$). SCA was determined by placing a drop of 3 μL of milliQ water on the surface using a needle and recording the images at 12 frames s^{-1} for 30 s while measuring the angle of the drop with the polymer surface. ACA was determined by placing the needle in the previously deposited drop and progressively adding water in order to observe an increase in the length of the baseline. RCA was determined by progressively removing the water with the needle until the drop was removed. RCA is the angle at which the baseline starts decreasing. Measurements were carried out using a Theta optical tensiometer (Biolin Scientific). X-ray photoelectron spectra were obtained at the National EPSRC XPS Users Service (NEXUS) at Newcastle University, an EPSRC Mid-Range Facility. XPS was performed using a K-Alpha apparatus (Thermo Scientific), with a microfocused monochromatic Al-K α source

(X-ray energy = 1486.6 eV) at a voltage of 12 kV, current of 3 mA, power of 36 W, and spot size of $400\ \mu\text{m} \times 800\ \mu\text{m}$. The analysis of the spectra and curve fitting were performed using CasaXPS software.

2.2. Fibronectin Conformation

The full FN conformation after adsorption on the polymeric samples and SAMs was observed using atomic force microscopy (AFM) and ELISA (enzyme-linked immunosorbent assay). For AFM, samples were coated with $20\ \mu\text{g mL}^{-1}$ of plasma human fibronectin (R&D Systems)/DPBS for 10 min and washed with DPBS and milliQ water. AFM was performed using a tapping-mode AFM (Nanowizard 3 from JPK) using cantilevers with a force constant of $3\ \text{N m}^{-1}$, a resonance frequency of 75 kHz, and a pyramidal tip, with radius of curvature less than 8 nm (MPP-21120 from Bruker, Billerica, MA). Several areas of the surface were scanned at different area sizes and line rates. The surface height, lock-in phase, and lock-in amplitude were observed. For ELISA, two primary antibodies were used: HFN7.1 (DSHB) and mAb1937 (Millipore) combined with HRP-Goat anti-mouse (Invitrogen) secondary antibody, which was coupled with a peroxidase for absorbance reading. FN coating was performed using the same protocol as explained above for AFM but for 1 h. Samples were washed with PBS, transferred to new 24-well plates, and then blocked with PBS BSA 1% w/v for 30 min at RT. Subsequently, samples were incubated with the primary antibodies for 1 h at RT and washed with PBS/Tween-20 0.5% v/v. The secondary antibody (HRP-Goat Anti-Mouse) was then added on all samples for 1 h at RT in the dark and washed with PBS/Tween-20 0.5% v/v. The substrate (color reagents A and B from R&D Systems) was then added for 20 min at RT, in the dark, stopped with a stop solution (R&D Systems), and transferred to a 96-well plate and absorbance was read at 450 nm and 550 nm.

2.3. Cell Attachment

DC (DU145 human prostate cancer cells) were thawed and re-suspended in Dulbecco's modified Eagle's medium (with $4.5\ \text{g L}^{-1}$ glucose and L-glutamine) with 1% v/v penicillin/streptomycin and 10% v/v fetal bovine serum (FBS; Life Technologies). Cells were grown at 37°C , 5% CO_2 , and harvested by trypsinization at 90% confluency. Attachment assay was done on samples sterilized for 20 min using a UV lamp and coated with FN at $20\ \mu\text{g mL}^{-1}$ for 1 h. Samples were then washed with PBS and seeded with cells at 1×10^4 cells per well for 3 h. Surfaces were washed twice with PBS to remove cells that were not firmly attached, fixed with formaldehyde 3.7% for 20 min at 4°C , and washed again. Samples were permeabilized for 5 min using a Triton X-100 based permeabilization buffer (0.5% v/v Triton X-100, 10.3% w/v saccharose, 0.292% w/v NaCl, 0.06% w/v MgCl_2 , and 0.476% w/v HEPES adjusted to pH 7.2) and mounted with vectashield with DAPI to stain the nuclei. Images were taken using an inverted epifluorescence microscope and the number of cells attached was determined using CellC total cell count analysis (Zeiss AXIO Observer Z1). In the case of blocking cell binding domains on FN, the same procedures were carried out using only samples coated with $20\ \mu\text{g mL}^{-1}$ of

FN and blocking the RGD and PHSRN sequences with HFN7.1 and mAb1937 at a 1:1 molar ratio ($14.6\ \mu\text{g mL}^{-1}$) for 1 h at room temperature.

2.4. Simulations

For the molecular dynamics (MD) simulations, the structures of the self-assembled monolayers (SAMs) molecules were drawn with the open source software Avogadro^[39]. The chains are defined as $\text{SH}(\text{CH}_2)_n\text{R}$, where R is $-\text{COOCH}_3$ and $-\text{COOCH}_2\text{CH}_3$ for the MA and EA terminated SAMs, respectively (Figure 1a). Two chain lengths, $n = 10$ and 18, have been investigated for both functional groups in order to test repeatability. The results for each of the two SAMs are quite similar, therefore in the main manuscript we report the findings from the $n = 10$ SAMs which we have studied experimentally. Analogous results for the $n = 18$ SAMs can be found in the Supporting Information. The SAM chains were parameterized with CGenFF^[40] for the all-atom forcefield CHARMM36^[41] with low penalties.

For each SAM, the GROMACS tool genconf^[42] was used to assemble 500 chains into a grid with an area per chain of $21.5\ \text{\AA}^2$. Each grid was then placed on a gold substrate with dimensions of $10.57\ \text{\AA} \times 10.18\ \text{\AA}$, which was modeled with the polarizable GolP-CHARMM forcefield^[43] with the sulfurs $2\ \text{\AA}$ away from the substrate. Atoms in the gold slab were frozen in all dimensions, except for the virtual atoms representing the charge. A steepest decent minimization was carried out with a $0.01\ \text{nm}$ initial step size and a target of $500\ \text{kJ mol}^{-1}\ \text{nm}^{-1}$ maximum potential force before the equilibration simulations were started. The NVT ensemble, which denotes a constant number of particles, volume, and temperature, was then used to equilibrate the system for 20 ns. During these simulations, the tilt of the EA and MA SAMs equilibrated to 59.2° and 60.0° , respectively (for the $n = 18$ variant see Table S1, Supporting Information).

A $9\ \text{nm}$ wide slab of water molecules modeled with the CHARMM36 TIP3P forcefield^[44] was added on top of the substrate. After the addition of water, the system energy was re-minimized and an NVT simulation of 1 ns was performed.

The FNIII 9-10 structure was extracted from the crystal structure (PDB 1FNF^[45]) to include the residue identifiers 1327–1415 for the 9th domain and 1416–1509 for the 10th domain. The interactions of the peptide were modeled with the CHARMM36 protein forcefield.^[41] The two domains were placed in the center of the simulation box in the xy plane and at a location in the z -dimension such that the closest atom in the protein was $20\ \text{\AA}$ from the SAM interface. The protein was oriented with its RGD motif facing away from the SAM surface. Water molecules within $2\ \text{\AA}$ of any atom in the protein were removed and the system was neutralized with one sodium ion (Na^+) due to the $-1e$ charge of the 10th domain. After removing the overlapping water molecules each of the four systems contained between 144 000 and 152 000 atoms. Figure 1b shows an example of the initial configuration of the peptide and the SAMs (water is not shown so the protein can be seen).

All simulations were carried out using the CHARMM36 forcefield (as described above) with the NVT parameters described earlier. The NVT ensemble was used because the parameterization of the polarizable gold substrate, GolP-CHARMM forcefield, was

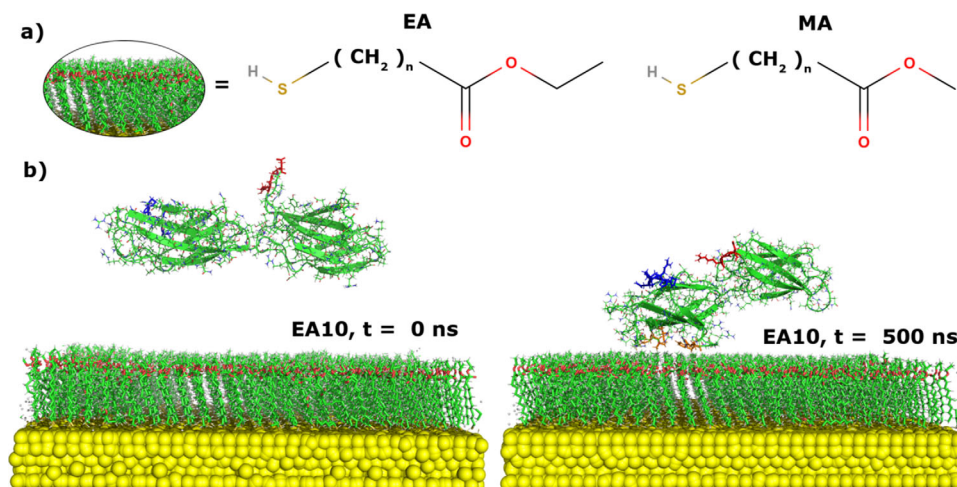


Figure 1. a) The structure of the four different molecules used to create the $n = 10$ or $n = 18$ SAMs. b) A snapshot of the $n = 10$ EA SAM and the peptide at the start of the simulation ($t = 0$ ns) and at the end of the simulation ($t = 500$ ns).

carried out in the same ensemble. The simulation box is periodic in the x - and y -dimensions and carbon walls were added to stop molecules from crossing the box in the z -dimension. The PME algorithm (Particle Mesh Ewald) which correctly accounts for the slab geometry of these simulation boxes was used to account for the long-range electrostatics. The temperature (300 K) was controlled by velocity rescaling algorithm^[46] containing a stochastic term, with a timestep of 2 ps. The cutoff for the van der Waals and Coulombic interactions was set to 1.2 nm and the LINCS constraint was applied to hydrogen-containing bonds.^[47] The GRO-MACS version 5.x MD package^[42] was used to simulate each of the four systems for 500 ns.

In order to investigate the hydration of EA and MA SAMs, additional simulations of the slab of water and the SAMs coated gold substrate were carried out following the same protocol for 50 ns.

2.5. Analysis

The open source package MDAnalysis^[48] was used to compute distances, coordination numbers, radial distribution functions (RDFs), and spatial density maps (SDMs). The electrostatic surface was computed with the PDB2PQR^[49] online service followed by APBS^[50] with default values and pH 7 for the two domains FNIII 9-10. The SDMs were visualized with VMD,^[51,52] the electrostatic maps were visualized with PyMOL,^[53] and other figures were created using Matplotlib.^[54]

The center of mass distance (COM) was calculated for each domain with respect to the nearest heavy atom (non-hydrogen) in the SAMs. We observe that a distance below 20 Å generally means that the domain is in contact with the SAM interface. However, due to the ellipsoidal shape of the domains, a COM-substrate distance of less than 20 Å is not sufficient to determine whether the domain is in contact with the substrate. In these cases, any claims of contact have been verified with VMD.

The radial distribution function (RDF) describe the radial distribution of one group of atoms around another group of atoms with respect to the density of the system, $g(r) = \frac{\rho(r)}{\rho}$, where ρ is

the global density of the object of interest and r the distance from the reference atom. To calculate the coordination number of oxygen atoms in the water molecules around a given atom, we determined the average number of oxygens within a given distance (e.g., the first neighbor distance as determined from the RDF) of that atom on the SAM over the course of the simulation.

Spatial density maps of the SAM hydration shells were created by superimposing the esters of EA and MA to first minimize the root mean square deviation. The rotational matrix transformation applied during the superimposition was also applied on the water oxygens found within a distance of 5.8 Å to the C20 atoms (see Figure 8). This distance is the first minimum in the RDF of water around the functional groups of EA and MA SAMs. The distribution of the oxygen atoms in the water molecules was discretized within a 3D grid and then normalised by the number of snapshots extracted before the generation of the density file. The isosurface shown in Figure 8b was created using the isovalue corresponding to the 95th percentile of the density of water around the MA functional group.

The exposure of the RGD motif is described by the relative distance of the COM of the motif and the COM of the peptide to the surface. Both domains were used for this calculation due to the position of the RGD motif on the loop between the two domains. A similar analysis was performed to determine the exposure of the PHSRN motif. However, in this case, the center of mass of the motif was compared to the center of mass of the 9th domain, as the PHSRN motif is found in that domain.

The python scripts used in the analysis and visualization have been uploaded to github (<https://github.com/Lorenz-Lab-KCL>).

3. Results

3.1. SAMs Are Chemically Similar to the Original Polymer Surfaces

Physicochemical characterization in the laboratory of self assembled monolayer samples was carried out to demonstrate that the SAMs were similar chemically to the polymeric samples.

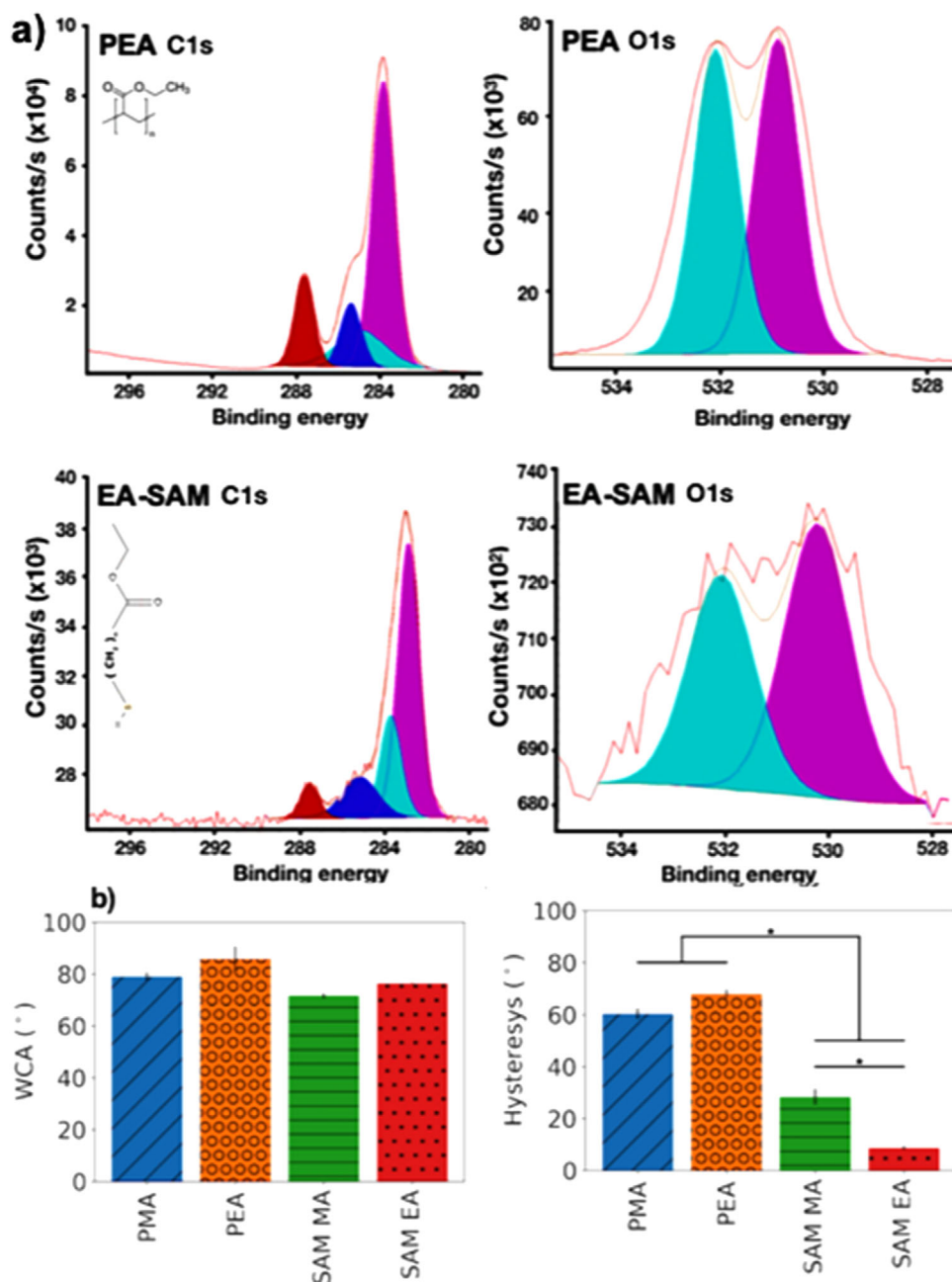


Figure 2. Physicochemical characterization of SAMs and polymeric samples in the laboratory. a) The graphs visualize the XPS spectrum for the EA SAMs ($n = 10$ chain length) and for the equivalent polymeric samples PEA. b) Water contact angle hysteresis in water. * represents a p -value of 0.01.

PEA and PMA samples were made using spin coating. The chemistry of PEA/PMA and EA/MA SAMs was confirmed using X-ray photoelectron spectroscopy (XPS). The self assembled monolayer spectrum shows overall a lower XPS signal for both C1s and O1s peaks. Both surfaces are classified as hydrophobic, with a static contact angle of around 75°, and similar behavior in dynamic contact angles, although PEA showed more hysteresis as defined by the difference between advancing and receding angles (**Figure 2**). Contact angle hysteresis has been interpreted as a measure of molecular mobility for surfaces that are chemically homogeneous and flat.^[55]

3.2. Adsorption of Fibronectin on EA and MA Surfaces

After production of self-assembled monolayers mimicking PEA and PMA, fibronectin (FN) was adsorbed on the surfaces. The molecular distribution of FN upon adsorption on the different SAMs can be obtained by AFM. **Figure 3** shows the organization of FN on the four surfaces (PEA, PMA, EA10, and MA10) after FN adsorption from a solution of $20 \mu\text{g mL}^{-1}$. FN conformation was similar on EA and PEA where a network conformation was observed, whereas the MA and PMA systems do not show any such network formation.

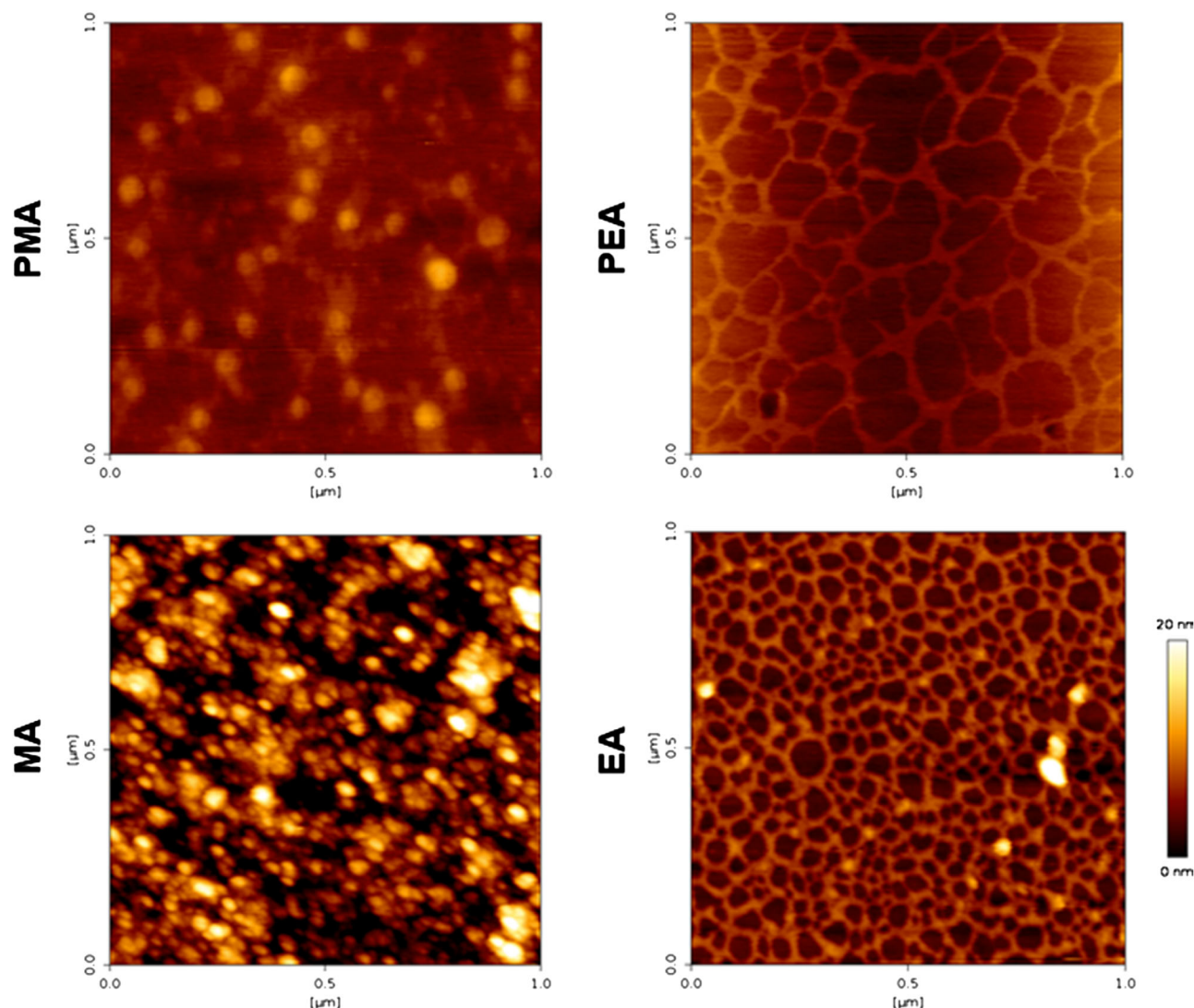


Figure 3. Atomic force microscopy images of fibronectin adsorbed on the different materials. A $20 \mu\text{g mL}^{-1}$ fibronectin solution was used to perform the coatings. Height signal is represented.

We then performed ELISAs to confirm that the conformation of fibronectin on the self assembled monolayers was the same as on the polymeric samples. The assay uses monoclonal antibodies, a well established method to probe for structural or conformational changes in adsorbed proteins.^[24] The antibodies used were directed against the flexible linker between the 9th and 10th type III repeats of FN (HFN7.1) and the synergy domain (mab1937).^[56] It has been previously demonstrated that HFN7.1 is a receptor-mimetic probe for integrin binding and cell adhesion.^[57]

As is observed in the **Figure 4**, SAMs EA10 and MA10 behave similarly to the polymeric samples PEA and PMA. The only difference found was that SAMs were able to present more RGD and PHSRN than the polymeric samples. It is important to notice that the carbon chain used to produce this self assembled monolayers was ten carbons long. Also, the FN is

adsorbed on the surface for 1 h to allow it to reach the adsorption equilibrium.

To go further and confirm a similar behavior between SAMs and polymeric samples during cell adhesion, we performed a short adhesion experiment blocking these domains. As we can see on **Figure 5**, on FN coated surfaces the number of cells attached were similar for all the samples, not showing differences among them. When the 9th and 10th type III domain was blocked using the HFN7.1 antibody, the number of cells attached was significantly decreased for the SAMs and for the polymeric samples, as has been previously shown for PEA and PMA.^[58] When the PHSRN domain was blocked the reduction on the number of cells attached was smaller in comparison when blocking the cell binding domain, as expected. In conclusion, we can confirm that the cells behave similar on the SAMs and on the polymeric samples.

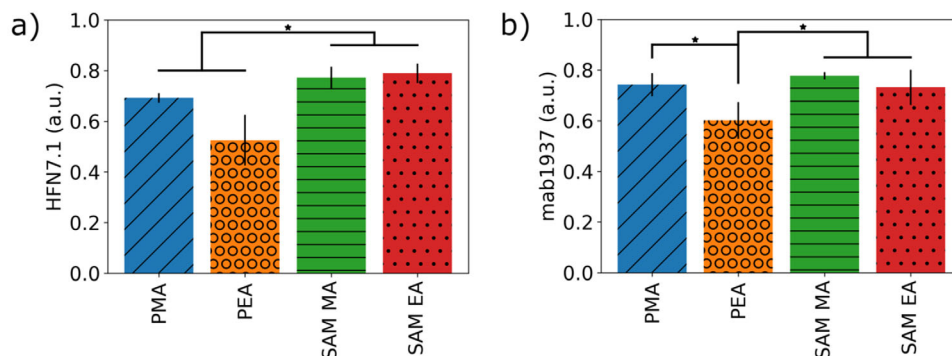


Figure 4. ELISAs analysis on SAMs and polymeric samples with fibronectin adsorbed using antibodies against the RGD [a] HFN7.1 antibody] and PHSRN [b] mab1937 antibody] motifs. * represents a *p*-value of 0.001.

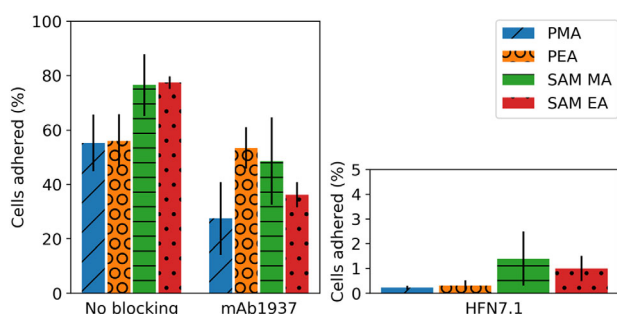


Figure 5. Short cell attachment on fibronectin-coated SAMs and polymeric samples in the absence or presence of antibodies against the RGD (HFN7.1 antibody) and PHSRN (mab1937 antibody) motifs.

3.3. Adsorption of FNIII 9 and 10 on EA and MA SAMs

In order to gain a more detailed understanding of how fibronectin interacts with the self-assembled monolayer interfaces, we have analyzed our all-atom molecular dynamics simulations of the FNIII 9 and 10 domains with the EA and MA interfaces. First, we calculated the minimum distance between the COM of each domain and the heavy atoms in the substrate (see Figure 6).

During the first half of the EA simulation, the 9th and 10th domain make contacts with the substrate. In the second half of the simulation, the 9th domain strengthens its adsorption and the 10th domain diffuses away from the surface. In the MA system, however, there is no adsorption taking place. Despite several short contacts made, primarily by the 10th domain, both domains diffuse away from the MA surface.

The adsorption of the 9th domain is divided into two periods: ea10pI and ea10pII. The period ea10pI spans the time $t = 10$ to 204 ns during which the 9th domain is in contact with the substrate but the fluctuation of the distance indicates lack of stability in the adsorption. At the end of the first period, the domain loses contact with the surface for ≈ 30 ns. After that, the domain stably adsorbs to the surface, and remains so over the entirety of period ea10pII ($t = 250$ to 500 ns). In contrast, in the MA system, the 9th domain never adsorbs to the SAMs, making only two brief contacts with the MA10 substrate at $t = 60$ to 93 ns and $t = 104$ to 148 ns.

The 10th domain does not adsorb to the substrate in the EA10 system. However, it makes two contacts during the first half of the simulation at $t = 70$ to 105 ns and 160 to 220 ns (yellow patches in Figure 6). During the first contact of the 10th domain, the 9th domain is weakly adsorbed but toward the end of the second contact, the 9th domain improves its adsorption. Once the 9th domain is adsorbed stably, the 10th domain predominantly stays away from the substrate. This suggests that the adsorption of the 9th domain is adversely affecting the adsorption of the 10th domain. In comparison, in the MA system, the 10th domain makes several contacts where the longest spans $t = 347$ to 422 ns, but this is followed by desorption of the protein.

The corresponding simulations with longer SAM chains ($n = 18$) show a consistent behavior. On EA18, the 9th domain similarly drives the adsorption, which in turn leads to the desorption of the 10th domain. The MA18 system follows the same behavior as well, with contacts made by the 10th domain which are followed by the domain diffusing away from the substrate (Figure S2, Supporting Information).

The AFM images (Figure 3) shows that the fibrillogenesis takes place on PEA and EA SAM, but not on PMA and MA SAM. Interestingly, in the relatively short simulations, we observe stable adsorption on EA SAMs ($n = 10$ and 18) but not on MA SAMs ($n = 10$ and 18). In the following section, we describe the role of different residues in the EA adsorption.

3.3.1. Key Residues in Adsorption Mechanism of FNIII 9 and 10 to EA SAMs

In order to better understand the interactions with the surface, we calculated the minimum distance between any heavy atom in each residue of the FN domains and any heavy atom in the SAM molecules. There are three overall trends in the EA system (Figure 6). First, the domains interact with the interface via the same regions: the residues clustered around PHE40 and SER80 in the 9th domain, and those found around GLY130 and SER170 in the 10th domain. Secondly, more residues in the 9th domain interact with the surface than from within the 10th domain. Thirdly, there is a clear relationship between the increase in the number of interacting residues in the 9th domain and the decrease in the 10th domain, which supports the idea that the interdomain interactions affect the adsorption.

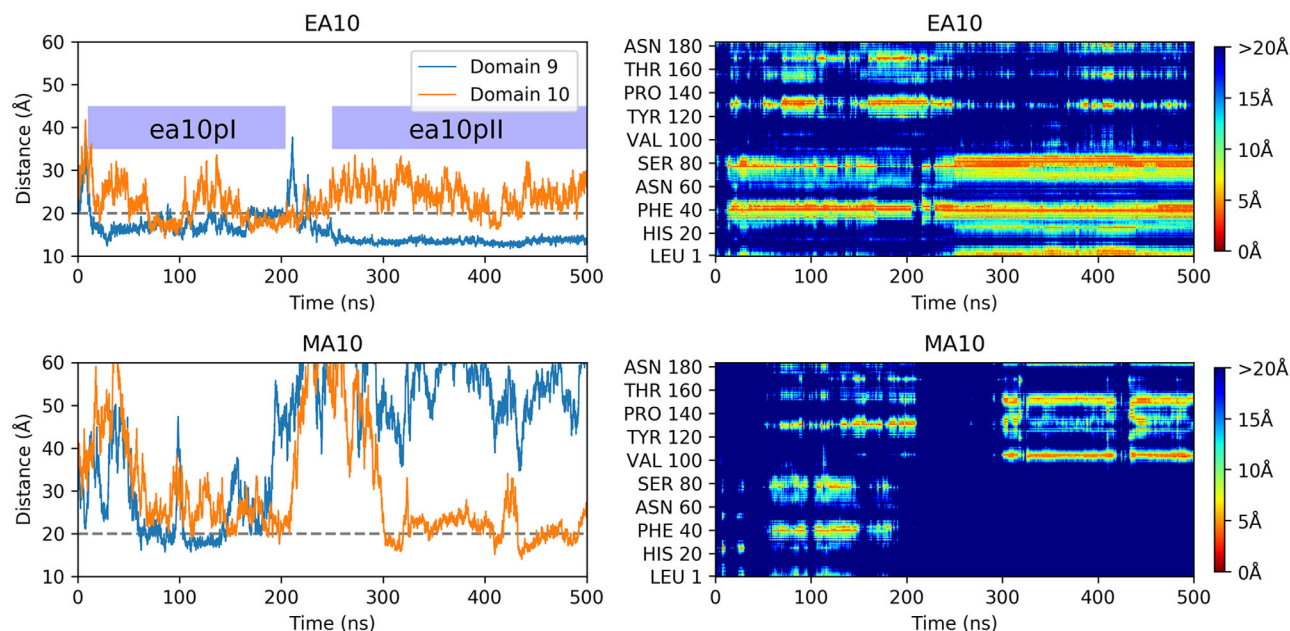


Figure 6. (Left) The distances from the center-of-mass of the 9th and 10th domains to the nearest heavy atoms in the SAMs over time. At a distance larger than 20 Å (grey dashed line) the domain is unlikely to be in contact with the substrate. (Right) The minimum distances between any heavy atom in each residue and any heavy atom in the SAMs over time.

Table 1. Residues less than 6 Å from the surface for at least 80% of the specified intervals.

SAM	Stage	Interval [ns]	Residues
EA10	ea10pI	10–204	PHE40, SER41, ARG43
	ea10pII	250–500	LEU1, HIS39, PHE40, GLU78, SER80, PRO81, LEU82, ILE84
MA10		326–416	PRO104, THR105, PRO153
		434–497	PRO104, THR105

The ea10pII stage represents the most stable adsorption period.

For each identified simulation period we list the key residues in the adsorption process extracted from the residue-surface distance maps, which are shown in Table 1 (and Table S2, Supporting Information). The region surrounding PHE40 has several residues adsorbing strongly to the surface, but only two are shared across the two EA systems. These two residues, HIS39 and PHE40 are common across the two strongly adsorbed periods ea10pII and ea18pII. Furthermore, PHE40 is the only residue that adsorbs strongly to the substrate during every period across the two systems. The fact that this strongly interacting residue is a phenylalanine suggests that hydrophobicity plays a role in the adsorption. During the stable adsorption period ea10pII, the main residues interacting with the surface are GLU78, SER80, PRO81, LEU82, and ILE84.

The 10th domain contacts both EA substrates sporadically. Some residues in the 10th domain, despite not qualifying as important residues by our criteria, show a propensity to stay close to the surface. Particularly, ASN131 which is even found close during the second half of the simulation. Other residues which tend

to come into contact with the surface include THR128, GLY129, GLY130, ASP156, and ASP169. These recurrent contacts suggest that the 10th domain attempts to adsorb to the surface. While we observe that the residue LEU1 at the N-terminal of the peptide, adsorbs, we do not believe this is of biological significance because this region of the peptide would be inaccessible due to the interdomain linker.

3.3.2. Interactions of the Peptide Backbone and Sidechains with the Surface

In order to understand the nature of the interacting residues (Table 1) that drive the adsorption of FNIII 9-10 to the EA SAMs, we check whether the residues interact with their side chains or backbones by calculating the minimum distances between them (COM) and any heavy atom within the EA SAMs. To focus on the residues that contribute the most to the adsorption, we consider only the 9th domain for both EA systems and its most stable adsorption period ea10pII (with ea18pII in the Supporting Information). For each selected residue (Table 1), a histogram of distances is shown in Figure S3, Supporting Information.

Between the two EA periods, we find only two common residues, HIS39 and PHE40. The last one is found predominantly close to the substrate in both systems, with its side chain always found closer than its backbone. The second most common residue, HIS39, has its backbone and side chain very close to the substrate on EA10.

During the period ea10pII, five residues are close to the surface: HIS39, PHE40, PRO81, LEU82, and to a lesser extent ILE84. Except for HIS39, they are all hydrophobic. Each of the five residues prefers to interact via its side chain. Similarly, SER80 has its backbone occasionally close to the substrate, but together

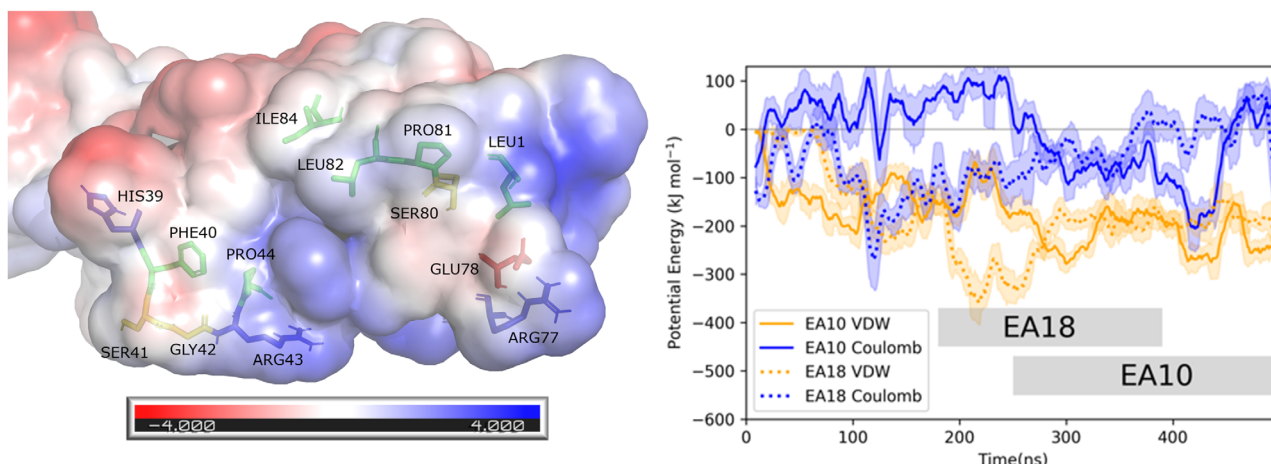


Figure 7. (Left) The electrostatic potential of the 9th domain with the bound residues labeled. The scale units are kT e⁻¹. (Right) The van der Waals and Coulomb potential energy of the protein interaction with the SAMs. The two grey blocks represent the most stably adsorbed periods ea10pII and ea18pII.

with GLU78, these residues show little specificity as their backbones and side chains are spread across the different distances.

During the period ea18pII, the residues closest to the surface are PHE40, GLY42, ARG43, and PRO44. Two of these, PHE40 and PRO44, are hydrophobic. The short distance of 3–4 Å seen in GLY42 is suspected to be due to its position between the other strongly adsorbed residues. Positively charged side chains of ARG43 and ARG77 are found relatively close to the substrate, but only ARG43 is close to the substrate throughout the whole period. The last residues, HIS39 and SER41 rarely interact with the substrate.

Across the EA10 and EA18 systems, besides the residue PHE40, there are four other hydrophobic residues which adsorb well to the surface. The only charged residues that can be distinguished is ARG43. The lack of specific interactions suggests the importance of hydrophobicity in the adsorption.

3.4. Energetics of Adsorption of FNIII 9 and 10 to EA SAMs

In order to better understand the effect of hydrophobicity in the adsorption process, we computed the peptide's surface electrostatic potential (Figure 7, left) and superimposed the important residues on the structure. The residues which we have identified as playing a key role in the adsorption mechanism are mostly found in the hydrophobic region between the negative (red) and positive (blue) regions. Rotation of the domain shows that behind HIS39 and ILE84 there is a more negatively charged patch, whereas on the opposite site, behind ARG43 and ARG77 we see a more positively charged region (not shown).

Two locations with more than one hydrophobic residue in the same area are found. The first region includes PRO81, LEU82, and ILE84 and it adsorbs strongly during ea10pII. The second is PHE40 with the adjacent PRO44, both which appear to drive the adsorption during ea18pII (Figure S3, Supporting Information).

We calculate the non-bonded potential energy terms consisting of van der Waals (vdW) and Coulomb terms for the protein–

surface interactions (Figure 7, right). The contribution of vdW interactions to the total potential energy is larger than that of Coulombic interactions across the two EA systems. It is therefore the vdW interactions between the residues and the EA substrates driving the adsorption which provides further evidence that the hydrophobic interactions play an important role in the adsorption of the 9th domain to the EA SAMs.

3.5. Hydration of the EA and MA SAMs

The loss of a single methylene bridge from the EA leads to a very different adsorption profile. Analysis of substrate hydration was performed for both MA and EA by calculating the radial distribution function (RDF) of the water oxygens around the SAMs double bonded oxygen (O2), single bonded oxygen (O1) and carbon (C20).

We present the RDF of the oxygen atoms in water molecules around the C20 carbon in the EA and MA functional groups in Figure 8a, where the difference in the hydration of these two terminal groups is apparent. The EA RDF has two distinctive hydration shells, with minima at 4.15 Å and 5.8 Å which represent the hydration shell of the carbonyl O2 and that of the ethyl group C20–C21, respectively. In contrast, the first MA hydration shell is much denser, as denoted by the larger magnitude of the first peak of the MA RDF, whose width nearly spans the two EA's RDF peaks.

To compare the hydration of the EA C20–C21 and MA C20, we used a spatial density map to visualize their most dense hydration regions in Figure 8b. The part of the hydration shell that shows the largest density disparity between the two functional groups, as previously described, is on top of the C20 and C21 atoms. The dense part of MA hydration shell (transparent blue) is much wider and covers the entire functional group. In contrast, the EA's hydration shell (yellow) is smaller in size, and has a gap between the carbonyl oxygen O2 and the C21 carbon. This gap represents a region of lower density, increasing the opportunity

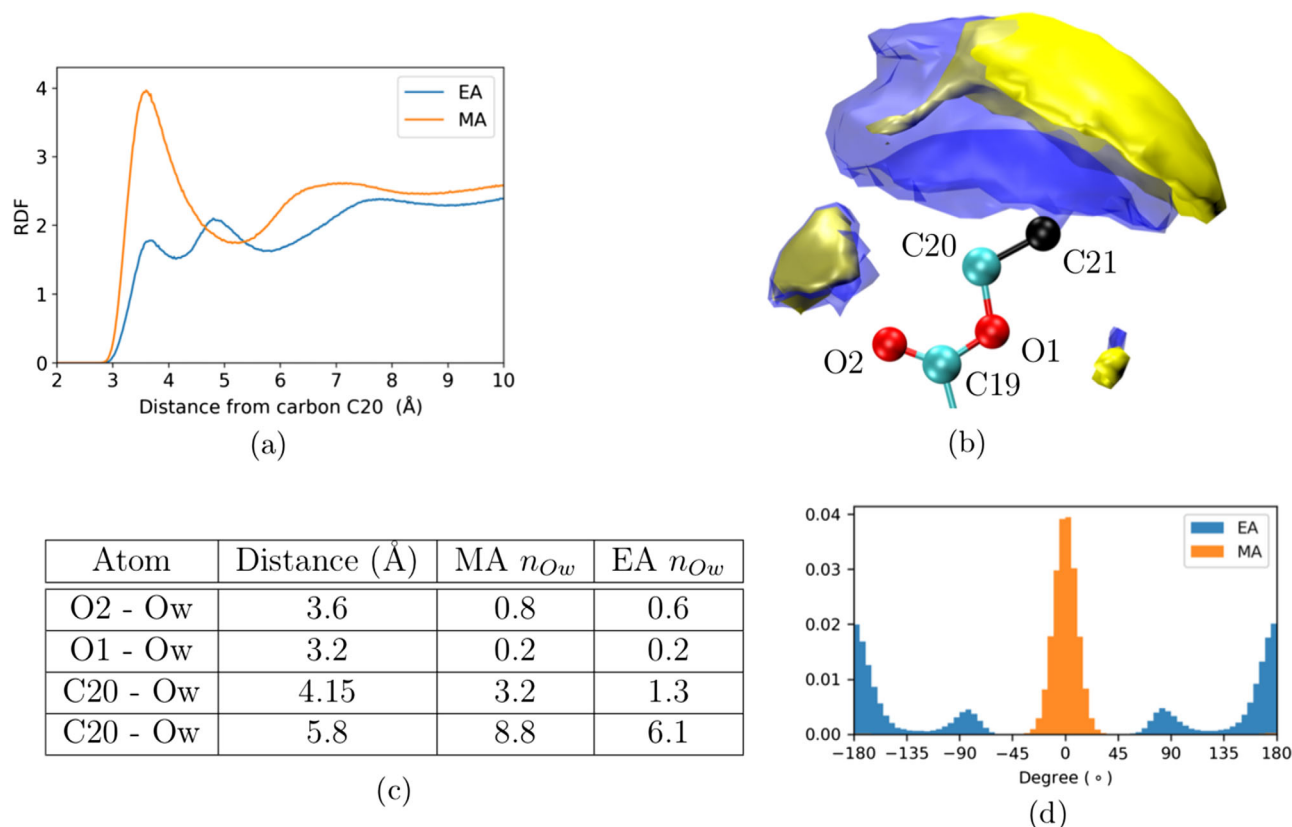


Figure 8. a) RDF of the oxygen atoms in the water molecules from the C20 carbon in the SAMs. b) Spatial density map of the oxygen atoms in the water molecules around the C20 atom for the MA (transparent blue) and EA (yellow) functional groups. The black atom represents a carbon atom present only in the EA functional group. c) Table of the nearest neighbor distance and coordination numbers for water molecules around various atoms within the EA and MA functional groups. d) Distribution of the terminal dihedral angles in the EA (O2-C19-O1-C20) and MA (C19-O1-C20-C21) headgroups, which show the rotation of the methyl group due to the extra methylene bridge.

to interact with the surface. Therefore, the MA functional group not only has a more dense hydration layer, but unsurprisingly, the visualized regions with the same density cutoff reveal that MA's hydration shell is larger in volume.

To quantify the difference in hydration between the two functional groups, we determine the coordination numbers (Figure 8c) by calculating the average number of water molecules found within a given distance. We find that EA's most polar atom, carbonyl O2, has a very similar coordination number to MA at the distance of 3.6 Å. The largest disparity is around the atom C20 where MA, at a radius of 4.15 Å, has on average 1.9 more water molecules than EA.

This difference between the EA and MA substrates is compounded by the extra methylene in EA which leaves less space for water. However, even at the longer radius of 5.8 Å, we observe further increase in the difference in the hydration, despite this region being not affected by the extra atom. The difference in hydration at 4.15 Å is 1.9 water molecules, whereas at 5.8 Å the difference increases to 2.7 water molecules. Thus the sole presence/lack of the extra methylene bridge is not sufficient to explain the difference in hydration between the two substrates.

Looking at the different conformations assumed by the functional groups, we find that due to the additional methylene bridge in the EA functional group, its methyl group rotates (Figure 8d).

This freedom to rotate stops the water molecules' ability to form denser hydration shells. In contrast, the MA functional group stays in the same plane of the ester group in both EA and MA functional groups, as shown with the single peak of the MA. The additional degrees of freedom of the EA methyl group results in a significantly different hydration, explaining how despite having only subtly different chemistry, the adsorption profile of the FNIII 9-10 domains is markedly different on the two substrates.

3.6. Exposure of RGD and PHSRN Motifs

The RGD and PHSRN motifs can be either buried in the surface or displayed for potential integrin binding, which determines the cellular response. To test whether the motifs are displayed, we measure whether the center of mass of each motif is closer to the surface than the center of mass of the peptide (Figure 9). In doing so, we find that the center of mass of each motif is generally farther away from the surface than the center of mass of the peptide after the peptide has adsorbed to the EA surface (Figure 9a). Therefore, the two motifs are exposed for binding with integrins. This is particularly clear for PHSRN which is consistently on display due to the 9th domain being well adsorbed.

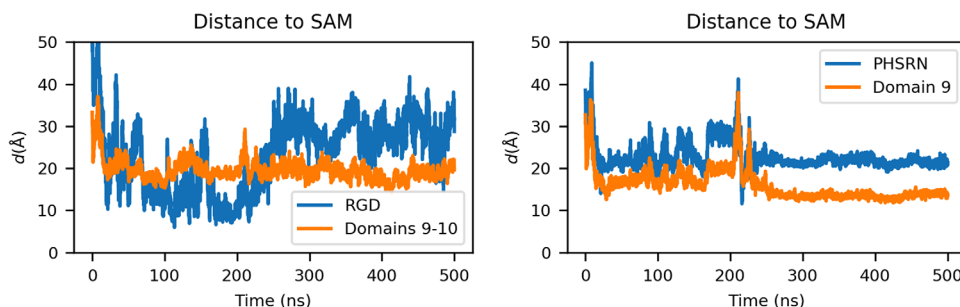


Figure 9. RGD and PHSRN motif exposure in the EA10 system. The shortest distances to the heavy atoms of the SAMs from the motif center of mass (RGD, PHSRN) and the protein fragment center of mass (domains 9 and 10, domain 9). The RGD loop, due to its location between the two domains, was compared to the center of mass of the whole protein fragment (domains 9 and 10). Meanwhile, the PHSRN motif was compared to the center of mass of the 9th domain. When the protein is closer to the surface than the motif, the motif is likely exposed to potential interactions.

RGD is similarly oriented away from the surface, although we see more fluctuations which we attribute to the flexible loop.

4. Discussion

Previously, we have shown that an additional methylene bridge in the polymer PEA leads to adsorbed FN forming a fibrillar network.^[26] Whereas, when FN adsorbed to the polymer PMA, the protein appears to aggregate. In this work we used SAMs functionalized with the EA and MA sidechains and show that FN behaves the same way with these interfaces (Figure 3).

We show that the SAMs mimic the polymers by comparing the surface hydrophobicity, chemical composition, and the interactions between FN and the different surfaces. The surfaces have been shown to be largely hydrophobic with the static contact angle of around 75°, and similar in the surface composition (Figure 2). ELISA was used to show that FN on the SAMs exposes the RGD and the PHSRN motifs to a similar extent, as probed by the HFN7.1 and mab1937 antibodies, respectively (Figure 4). This orientation of adsorbed FN is of importance to the cell adhesion. By blocking the RGD region with the HFN7.1 antibody, it is shown that the cell adhesion is stopped on SAMs and polymers, showing consistent results across the surfaces. In order to understand how the small difference in the surface chemistry leads to network formation, we have used all-atom molecular dynamics simulations to model the interaction between the RGD and PHSRN containing 9th and 10th domains of FNIII and the EA and MA SAMs.

Our simulations show that the adsorption of FNIII 9 and 10 takes place on the EA SAM, on which the fibrillogenesis takes place. However, no adsorption occurred on the MA SAM (Figure 6) on which fibrillar networks are absent. The adsorption of the two domains on EA SAMs shows that both RGD and PHSRN motifs are exposed (Figure 9), which the ELISA experiments have previously established. The simulations show that the adsorption is mostly due to the van der Waals interactions. This adsorption is driven by a hydrophobic region in the surface of the protein (Figure 7). This is in agreement with the Water Contact Angle experiment which showed that the substrates are largely hydrophobic. The adsorption (or lack thereof), motif exposure, and the nature of the interaction of the FNIII 9 and 10 on two different hydrocar-

bon chain lengths ($n = 10$ and 18) of EA and MA SAMs showed similar behavior.

In comparison to previous simulation studies of FNIII domains adsorbing to different SAMs coated substrates, our results show some interesting similarities and differences. The most significant difference is that in most of the other simulation studies,^[32,33,35] the peptides were reported to adsorb to all surfaces, whereas in our studies we observe the peptides to adsorb to EA SAMs but not the MA SAMs. Additionally, in our simulations we observe that there is specific binding between the two domains to the EA SAMs, as the same residues are involved in the two simulations we have conducted. In the previous simulation studies of the FNIII 10th, 9th and 10th,^[33] and 8–10th^[35] domains all showed slightly different residues being key in the adsorption to uncharged interfaces and therefore different orientations of the peptides. Li et al. found that the FNIII 10th and 9th and 10th domains both adsorb such that the RGD and PHSRN motifs are available for cell binding^[33] whereas Liamas found that nonspecific binding of the 8–10th domains leads to these motifs not consistently being available.^[35] Therefore, when considering the results presented in this work and the others, it is clear that the chemistry of the functional groups of the SAMs play a significant role in the structure and functionality of the adsorbed FN, and that there can be significant differences even within a certain broad classification of interfaces that are produced (e.g., uncharged).

The qualitative comparison of the simulations and the experiments agrees to a large extent leading us to the question of what is the difference between the two substrates and how it defines whether FN forms fibril networks. The simulations show that EA SAMs exhibit significantly denser local hydration shells than MA SAMs. We visualized the hydration to show that the MA SAMs hydration shell is larger in volume and more dense. We find that the single extra methylene bridge introduces additional degrees of freedom in the EA functional group, allowing the methyl group to rotate and disrupt the hydration shell. In contrast, the MA functional group stays in a single plane and allows for better ordering of the hydrating water molecules (Figure 8). Previously, we have shown experimentally that the adhesion strength of fibronectin on PMA is significantly less than that of fibronectin adsorbed on PEA,^[59] which is consistent with these simulation findings. Therefore, we conclude that FN is less likely to interact with the MA surface because the hydration layer of

water molecules is more difficult to penetrate. The experimentally observed FN aggregates might simply be due to FN–FN interactions being stronger than the FN–MA interactions.

Supporting Information

Supporting Information is available from the Wiley Online Library or from the author.

Acknowledgements

The authors thank Rachel Love and Zhe A. Cheng for experimental support. M.K.B. and C.D.L. acknowledge the support by the Francis Crick Institute which receives its core funding from Cancer Research UK (FC001179), the UK Medical Research Council (FC001179), and the Wellcome Trust (FC001179). Additionally, M.K.B. acknowledges the valuable conversations he had with Willie Taylor and Enrico Spiga at the Francis Crick Institute during the course of this study. Via the authors' membership of the UK's HEC Materials Chemistry Consortium, which is funded by EPSRC (EP/L000202/1, EP/R029431/1), this work used the ARCHER UK National Supercomputing Service (<http://www.archer.ac.uk>) and the UK Materials and Molecular Modelling Hub (MMM Hub) for computational resources, which is partially funded by EPSRC (EP/P020194/1) to carry out the MD simulations reported in this manuscript. This study was supported by the UK Regenerative Medicine Platform (MRC Grant MR/L022710/1) and the UK Engineering and Physical Sciences Research Council (EPSRC EP/P001114/1). X-ray photoelectron spectroscopy was conducted by the National EPSRC XPS Users' Service (NEXUS), Newcastle.

Conflict of Interest

The authors declare no conflict of interest.

Keywords

fibrillogenesis, fibronectin, material-driven fibrillogenesis, molecular dynamics, surface hydration

Received: August 28, 2019
Revised: September 27, 2019
Published online: October 28, 2019

- [1] E. L. George, E. N. Georges-Labouesse, R. S. Patel-King, H. Rayburn, R. O. Hynes, *Development* **1993**, 119, 1079.
- [2] M. Salmerón-Sánchez, P. Rico, D. Moratal, T. T. Lee, J. E. Schwarzbauer, A. J. García, *Biomaterials* **2011**, 32, 2099.
- [3] J. Sottile, D. C. Hocking, K. J. Langenbach, *J. Cell Sci.* **2000**, 113, 4287.
- [4] C. M. Williams, A. J. Engler, R. D. Slone, L. L. Galante, J. E. Schwarzbauer, *Cancer Res.* **2008**, 68, 3185.
- [5] R. Pankov, *J. Cell Sci.* **2002**, 115, 3861.
- [6] J. E. Schwarzbauer, *J. Cell Biol.* **1991**, 113, 1463.
- [7] S. E. D'Souza, M. H. Ginsberg, E. F. Plow, *Trends Biochem. Sci.* **1991**, 16, 246.
- [8] S. Aota, M. Nomizu, K. M. Yamada, *J. Biol. Chem.* **1994**, 269, 24756.
- [9] S. D. Redick, D. L. Settles, G. Briscoe, H. P. Erickson, *J. Cell Biol.* **2000**, 149, 521.
- [10] B. Geiger, A. Bershadsky, R. Pankov, K. M. Yamada, *Nat. Rev. Mol. Cell Biol.* **2001**, 2, 793.
- [11] V. Vogel, *Annu. Rev. Physiol.* **2018**, 80, 353.
- [12] K. J. Johnson, H. Sage, G. Briscoe, H. P. Erickson, *J. Biol. Chem.* **1999**, 274, 15473.
- [13] L. M. Maurer, W. Ma, D. F. Mosher, *Crit. Rev. Biochem. Mol. Biol.* **2016**, 51, 213.
- [14] A. Maqueda, J. V. Moyano, M. Hernández del Cerro, D. M. Peters, A. Garcia-Pardo, *Matrix Biol.* **2007**, 26, 642.
- [15] D. C. Hocking, J. Sottile, P. J. McKeown-Longo, *J. Biol. Chem.* **1994**, 269, 19183.
- [16] D. C. Hocking, *J. Cell Biol.* **1996**, 133, 431.
- [17] C. Wu, V. M. Keivens, T. E. O'Toole, J. A. McDonald, M. H. Ginsberg, *Cell* **1995**, 83, 715.
- [18] C. Zhong, M. Chrzanowska-Wodnicka, J. Brown, A. Shaub, A. M. Belkin, K. Burridge, *J. Cell Biol.* **1998**, 141, 539.
- [19] S. Miyamoto, S. K. Akiyama, K. M. Yamada, *Science* **1995**, 267, 883.
- [20] J. L. Sechler, Y. Takada, J. E. Schwarzbauer, *J. Cell Biol.* **1996**, 134, 573.
- [21] P. Singh, C. Carraher, J. E. Schwarzbauer, *Annu. Rev. Cell Dev. Biol.* **2010**, 26, 397.
- [22] D. Gugutkov, C. González-García, J. C. Rodríguez Hernández, G. Altankov, M. Salmerón-Sánchez, *Langmuir* **2009**, 25, 10893.
- [23] R. Emch, F. Zenhausern, M. Jobin, M. Taborelli, P. Descouts, *Ultramicroscopy* **1992**, 42–44, 1155.
- [24] V. Llopis-Hernández, M. Cantini, C. González-García, Z. A. Cheng, J. Yang, P. M. Tsimbouri, A. J. García, M. J. Dalby, M. Salmerón-Sánchez, *Sci. Adv.* **2017**, 2, 1600188.
- [25] Z. A. Cheng, A. Alba-Perez, C. González-García, H. Donnelly, V. Llopis-Hernández, V. Jayawarna, P. Childs, D. W. Shields, M. Cantini, L. Ruiz-Cantu, A. Reid, J. F. C. Windmill, E. S. Addison, S. Corr, W. G. Marshall, M. J. Dalby, M. Salmerón-Sánchez, *Adv. Sci.* **2019**, 6, 1800361.
- [26] F. Bathawab, M. Bennett, M. Cantini, J. Reboud, M. J. Dalby, M. Salmerón-Sánchez, *Langmuir* **2016**, 32, 800.
- [27] C. Liao, Y. Xie, J. Zhou, *RSC Adv.* **2014**, 4, 15759.
- [28] K. Kubiak-Ossowska, P. A. Mulheran, W. Nowak, *J. Phys. Chem. B* **2014**, 118, 9900.
- [29] G. Raffaini, F. Ganazzoli, *Langmuir* **2004**, 20, 3371.
- [30] C. Wu, M. Chen, C. Xing, *Langmuir* **2010**, 26, 15972.
- [31] X. Wang, Z. Li, H. Li, S. Ruan, J. Gu, *J. Mater. Sci.* **2017**, 52, 13512.
- [32] H. Wang, Y. He, B. D. Ratner, S. Jiang, *J. Biomed. Mater. Res. A* **2006**, 77A, 672.
- [33] T. Li, L. Hao, J. Li, C. Du, Y. Wang, *Langmuir* **2018**, 34, 9847.
- [34] K. Wilson, S. J. Stuart, A. Garcia, R. A. Latour Jr, *J. Biomed. Mater. Res. A* **2004**, 69A, 686.
- [35] E. Lamas, K. Kubiak-Ossowska, R. A. Black, O. R. T. Thomas, Z. J. Zhang, P. A. Mulheran, *Int. J. Mol. Sci.* **2018**, 19, 3321.
- [36] M. Panos, T. Z. Sen, M. G. Ahunbay, *Langmuir* **2012**, 28, 12619.
- [37] S. Regis, S. Youssefian, M. Jassal, M. D. Phaneuf, N. Rahbar, S. Bhowmick, *J. Biomed. Mater. Res. A* **2014**, 102, 1697.
- [38] G. Raffaini, F. Ganazzoli, *Phys. Chem. Chem. Phys.* **2006**, 8, 2765.
- [39] M. D. Hanwell, D. E. Curtis, D. C. Lonie, T. Vandermeersch, E. Zurek, G. R. Hutchison, *J. Cheminformatics* **2012**, 4, 17.
- [40] K. Vanommeslaeghe, E. P. Raman, A. D. MacKerell Jr, *J. Chem. Inf. Model.* **2012**, 52, 3155.
- [41] R. B. Best, X. Zhu, J. Shim, P. E. M. Lopes, J. Mittal, M. Feig, A. D. MacKerell Jr, *J. Chem. Theory Comput.* **2012**, 8, 3257.
- [42] M. J. Abraham, T. Murtola, R. Schulz, S. Páll, J. C. Smith, B. Hess, E. Lindahl, *SoftwareX* **2015**, 1–2, 19.
- [43] L. B. Wright, P. M. Rodger, S. Corni, T. R. Walsh, *J. Chem. Theory Comput.* **2013**, 9, 1616.
- [44] W. L. Jorgensen, J. Chandrasekhar, J. D. Madura, R. W. Impey, M. L. Klein, *J. Chem. Phys.* **1983**, 79, 926.
- [45] D. J. Leahy, I. Aukhil, H. P. Erickson, *Cell* **1996**, 84, 155.

- [46] G. Bussi, D. Donadio, M. Parrinello, *J. Chem. Phys.* **2007**, 126, 014101.
- [47] B. Hess, H. Bekker, H. J. C. Berendsen, J. G. E. M. Fraaije, *J. Comput. Chem.* **1997**, 18, 1463.
- [48] R. J. Gowers, M. Linke, J. Barnoud, T. J. E. Reddy, M. N. Melo, S. L. Seyler, J. Domański, D. L. Dotson, S. Buchoux, I. M. Kenney, O. Beckstein, *Proc. of the 15th Python in Science Conf.* **2016**, pp. 98–105, <http://conference.scipy.org/proceedings/scipy2016/>.
- [49] T. J. Dolinsky, J. E. Nielsen, J. A. McCammon, N. A. Baker, *Nucleic Acids Res.* **2004**, 32, 665.
- [50] N. A. Baker, D. Sept, S. Joseph, M. J. Holst, J. A. McCammon, *Proc. Natl. Acad. Sci. USA* **2001**, 98, 10037.
- [51] W. Humphrey, A. Dalke, K. Schulten, *J. Mol. Graph. Model.* **1996**, 14, 33.
- [52] J. Stone, *Master's Thesis*, Computer Science Department, University of Missouri-Rolla **1998**.
- [53] The PyMOL Molecular Graphics System, Version 1.8, Schrödinger, LLC.
- [54] J. D. Hunter, *Comput. Sci. Eng.* **2007**, 9, 90.
- [55] M. Cantini, P. Rico, D. Moratal, M. Salmerón-Sánchez, *Soft Matter* **2012**, 8, 5575.
- [56] R. C. Schoen, K. L. Bentley, R. J. Klebe, *Hybridoma* **1982**, 1, 99.
- [57] K. E. Michael, V. N. Vernekar, B. G. Keselowsky, J. C. Meredith, R. A. Latour, A. J. García, *Langmuir* **2003**, 19, 8033.
- [58] F. A. Vanterpool, M. Cantini, F. P. Seib, M. Salmerón-Sánchez, *BioResearch Open Access* **2014**, 3, 286.
- [59] C. González-García, M. Cantini, J. Ballester-Beltrán, G. Altankov, M. Salmerón-Sánchez, *Acta Biomater.* **2018**, 77, 74.